

Downlink Receiver Algorithms for Deep Space Optical Communications

Meera Srinivasan, Ryan Rogalin, Norman Lay, Matthew Shaw, and Andre Tkacenko

Jet Propulsion Laboratory, California Institute of Technology, 4800 Oak Grove Drive,
Pasadena, CA, USA

ABSTRACT

The goal of the Deep Space Optical Communications project at the Jet Propulsion Laboratory is to demonstrate laser communication links at ranges out to approximately 3 AU. In this paper, we discuss a downlink receiver concept capable of demodulating optical pulse-position modulated (PPM) waveforms with data rates varying from approximately 50 kbps up to 265 Mbps, using a range of PPM orders, slot widths, and code rates. The receiver operates on recorded timestamps corresponding to the times-of-arrival of photons detected by a photon-counting detector array followed by a commercial time-tagger. Algorithms are presented for slot, symbol, and frame synchronization as well as parameter estimation. Estimates of link performance are evaluated through Monte-Carlo simulation for an optical channel that includes optical losses, detector blocking, signal clock dynamics, and pointing-induced downlink fades. Based upon these simulation results, it is expected that link closure may be achieved with at least 3 dB of margin under a variety of relevant conditions.

1. INTRODUCTION

Deep space optical communication links require the use of photon counting detectors and receivers capable of demodulating pulse-position modulation (PPM) signals in a photon starved channel.¹ To communicate across this channel the photodetector must be capable of detecting individual photons, which are then counted by the receiver and converted into statistics appropriate for signal demodulation and decoding. The Deep Space Optical Communications project at the Jet Propulsion Laboratory uses tungsten silicide superconducting nanowire single photon detector (WSi SNSPD) arrays in order to achieve photon-efficient communications.^{2,3} These devices have high single photon detection efficiency, low detector jitter, and an active area suitable for coupling to large diameter ground telescopes. Coupled with custom detector readout circuitry and high speed data acquisition electronics, this detector/receiver architecture is capable of processing modulation bandwidths in the GHz range. The job of the downlink receiver assembly is to aggregate the photon arrival information from the SNSPD detector array and estimate the number of detected signal photons per PPM slot, temporally align the signal, generate the log-likelihood ratios (LLRs) for information decoding, and provide suitable parameter estimates necessary for other control and diagnostic subsystems.

In pulse-position modulation, the transmit laser is pulsed on during one of M time slots, forming a transmitted symbol that conveys $\log_2(M)$ bits of information. In order to demodulate this signal, the receiver must align its own slot clock to that of the received waveform to count the number of arrivals within each slot. As the output of each element in the SNSPD array is an electrical pulse signifying a detected photon arrival, a typical receiver architecture might utilize a number of high speed analog-to-digital (ADC) converters to generate data samples proportional to the number of detected photon counts on each detector channel. Due to the bandwidth expansion factor of PPM, this approach requires large sampling rates in order to handle higher rate modulation, even if just one sample per PPM slot is used along with phase adjustment of the sample clock.⁴ In addition, the SNSPD array consists of at least 64 pixels in order to overcome detector blocking and accommodate the photon flux rates needed to close high data rate links. While the pixel outputs may be combined in order to reduce the number of channels needing to be processed, this requires cryogenic electronics development and time distribution and alignment across a large temperature gradient, contributing to receiver complexity and

Further author information: (Send correspondence to Meera Srinivasan)
E-mail: msrini@jpl.nasa.gov, Telephone: 1 818 354 0097

performance losses. In this paper, an alternative approach is described that utilizes a commercial FPGA-based multi-channel time-to-digital converter (TDC) as the digital data capture mechanism. These time-to-digital converters are used in LIDAR and high energy physics applications⁵ to provide very high resolution time-of-arrival information, but have not typically been designed to handle the photoelectron count rates required for higher rate optical communications. Current efforts are therefore focusing upon adapting TDC technology to handle the count rates, channels, and data interfaces needed for use in communications signal processing.

Demodulating an optical PPM signal from unsynchronized detected photon time-of-arrival data requires the estimation of the number of detector pulses within a specified time interval, estimation of the received signal slot and symbol timing, and interpolation of the sample counts to produce slot likelihood ratios for information decoding in the presence of transmitter clock dynamics. Other tasks include alignment of code frames, parameter estimation, deinterleaving, and decoding. We begin in Section 2 with an overview of the downlink signal format and receiver functions. This is followed in Section 3 with descriptions of the estimation and synchronization algorithms. In Section 4, results comparing the system performance to that of an ideal Poisson counting receiver for representative deep space operating points are given.

2. SYSTEM OVERVIEW

The DSOC downlink data signaling format⁶ is designed to achieve power efficiency along with low implementation complexity on the space terminal transmitter. It supports a wide range of downlink data rates through the adjustment of a variety of signaling parameters. DSOC data sources produce frames consisting of header, information, and cyclic redundancy check (CRC) bits, which are protected with serially-concatenated convolutionally-coded PPM (SCPPM) error-correction codes.⁷ One of three code rates ($1/3, 1/2, 2/3$) and four PPM orders (16, 32, 64, 128) may be selected. The M -bit encoded PPM symbols are then interleaved using periodic convolutional channel interleaving, with a frame alignment sequence (FAS) inserted between each codeword's worth of interleaved symbols. The channel interleaver has row and relative delay parameter settings that may be varied in combination with the other signal parameter values to yield an interleaving depth appropriate to the given channel conditions. The frame alignment sequence facilitates low-complexity deinterleaver and codeword synchronization.

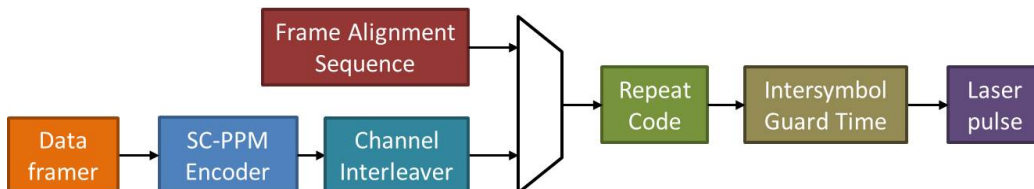


Figure 1: SCPPM signal structure

Two other adjustable signaling parameters are the PPM pulse width and the symbol repeat factor. These parameters together determine the effective PPM slot width, which is adjusted to support link closure under different background conditions. At low background levels, a narrower slot width results in more efficient signaling, but is limited to the bandwidth that can be supported by the receiver. As the background level increases, the slot width must increase in order to collect more signal photons to support the link, but is constrained by limits on the downlink laser pulse width. This limitation is overcome through symbol repetition, in which each PPM symbol is consecutively repeated Q times. This effectively increases the slot width, as the mean number of signal photons collected after the repeated symbol statistics are combined in the receiver is theoretically equal to the mean number of photons collected over a single longer slot. For DSOC, pulse widths vary from 0.5 to 8 ns, while symbol repeat factors up to 32 are expected to be sufficient for projected operating conditions.

One last notable aspect of the DSOC modulation format is the use of intersymbol guard time⁸ for PPM slot and symbol synchronization. With intersymbol guard time, an additional P non-signal slots are appended to the end of each PPM symbol, so that each symbol consists of $M + P$ slots. Because no signal pulses are transmitted in the guard time slots, statistics from these intervals may be used to estimate symbol and slot phase and frequency. In DSOC the number of guard time slots is specified as $P = M/4$.

Given this signal format, the DSOC downlink receiver must synchronize the received data to the DSOC symbol frames while compensating for transmitted clock phase and frequency dynamics, strip off the intersymbol guard slots, estimate signal and background parameters and form log-likelihood ratios, estimate symbol repetition boundaries and combine repeated symbol LLRs, estimate codeword frame boundaries and remove frame alignment sequences, de-interleave the subchannel symbols, decode the data, and return the information bits. Algorithms for performing these functions are described in the next section.

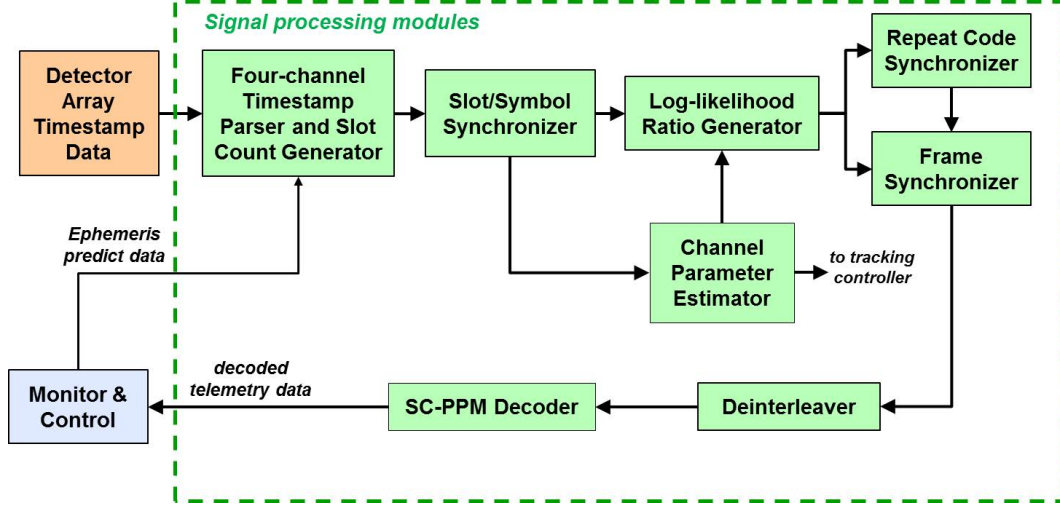


Figure 2: Deep space optical communications flight terminal pointing and tracking concept

3. ALGORITHMS

3.1 Time-to-Digital Output Processing

In order to perform the functions described in the system overview, the receiver must generate likelihoods ratios (or approximations) for estimation and decoding. The output of the TDC consists of timestamps whose bits are allocated to identification of the detected photoelectron time-of-arrival and SNSPD pixel channel number. In a photon-starved environment, transmission of timestamps may be more bandwidth efficient than traditional fixed rate sampling of the detector output waveform. For example, if SNSPD pixels are combined into four quadrants (in order to facilitate spatial tracking of the downlink beam spot on the SNSPD array) and four one-bit 6 GHz ADCs are used, a constant 24 Gbps data bandwidth must be handled at the front-end of the digital receiver assembly. In contrast, a TDC-based digital acquisition system with 32-bit timestamps will generate a variable data bandwidth depending upon the operating scenario. In a high data rate scenario with insignificant background and an average detected signal count rate of 400 Megacounts per second would require a TDC output bandwidth of 12.8 Gbps, while a lower data rate scenario dominated by a detected background count rate of 30 Megacounts per second would result in a timestamp output rate of just 1 Gbps.

In the DSOC downlink receiver architecture, the timestamps for each detected photon arrival are parsed and collected across detector channels to form sparse count and index data. The sparse count and index data indicate the number of counts within a timestamp resolution interval and the index of that nonzero count interval. Note that the indices for the timestamp will rollover after some period; for example, if 24 bits are allocated to represent 166 picosecond timestamp resolution time-of-arrival, the rollover time would be approximately 2.8 ms. To resolve the rollover ambiguity, a fiducial pulse periodic with the rollover time could be injected on an additional TDC channel as a time reference. As timestamps are streamed out of the TDC, they are binned into 166 ps intervals. The sparse index and corresponding counts for the nonzero bins may then be used in slot and symbol synchronization and log-likelihood ratio formation.

3.2 Slot and Symbol Synchronization

A method for estimating PPM symbol timing offset using signaling with intersymbol guard time has been developed and characterized in prior work.⁸ This algorithm utilizes cyclically accumulated slot count statistics as the set of observables from which to extract timing information via a simple correlation, which is low complexity but suboptimal. More recently, the maximum likelihood timing offset estimator given these same observables has been derived⁹ and shown to approach the Cramér-Rao bound while maintaining low implementation complexity, under the assumption that the slot statistics are Poisson distributed.

For a PPM+ISGT symbol of length T_{sym} , the symbol is divided into $M+P$ slots of length $T_{slot} = T_{sym}/(M+P)$, and messages of length $\log_2 M$ are encoded by sending an optical pulse in one of the first M slots, while the remaining P slots do not contain signal pulses. We assume the use of a photon-counting optical detector. The output process of such a detector is well-modeled as a Poisson point process whose mean is proportional to the incident light on the detector.¹⁰ The mean number of counts may be non-linearly proportional to the incident light due to phenomena such as blocking,¹¹ but we assume that the large number of detector pixels is sufficient to overcome significant deviations from the Poisson model. We observe the detector time-of-arrival process over N symbols, and from that form the count process $x[n]$, as described in Section 2. For Poisson distributed counts, the sum of the counts per slot provides a sufficient statistic for the timing offset. Thus the indices of $x[n]$ range in $n \in \{0, \dots, (M+P)N - 1\}$. The variable N may be increased to collect signal flux for a sufficient amount of time in order to be able to distinguish signal slots from ISGT slots, but is limited by the discrepancy between the transmitter and receiver clock frequencies. In practice the integration time is limited to a duration over which the timing offset may be assumed to be constant. The observations are binned over this time into a vector \mathbf{y} such that $y_m = \sum_{i=0}^{N-1} x[m+iN]$ with $m \in \{0, \dots, M+P-1\}$.

Given the observable \mathbf{y} , the maximum likelihood estimate of the symbol timing offset τ was derived⁹ as

$$\hat{\tau}_{ML} = \arg \max_{\hat{\tau}_{ML,j}} \ell(\hat{\tau}_{ML,j}; \mathbf{y}) \quad (1)$$

where

$$\hat{\tau}_{ML,j} = \frac{\frac{N}{M} K_s ((j+1)y_{M+j+1} + jy_j) + NK_b(y_{M+j} - y_j)}{\frac{N}{M} K_s(y_{M+j} + y_j)}, \quad (2)$$

and the likelihood function $\ell(\hat{\tau}_{ML,j}; \mathbf{y})$ is given by

$$\ell(\tau; \mathbf{y}) = \sum_{m=0}^{M+P-1} y_m \log \lambda_m((\tau - m) \bmod (M+P)), \quad (3)$$

where K_s is the mean number of detected signal counts per PPM symbol, K_b is the mean number of detected background counts per PPM slot, and $\lambda_m(\tau) = \frac{N}{M} K_{s,m}(\tau) + NK_b$ is a detected count flux intensity function as a function of the timing offset τ . Thus, the timing estimate can be formed by calculating $2(M+P)$ simple algebraic equations and evaluating a maximum over $M+P$ quantities. In comparison, the correlation-based method⁸ accumulates the slot counts of the P adjacent bins to form a “superslot” count vector \mathbf{z} of length $\frac{M+P}{P}$, i.e. $z_j = \sum_{i=0}^{P-1} y_{jP+i}$ (assuming that $(M+P) \bmod P = 0$), and then forms the integer and fractional estimates of the timing offset as:

$$\hat{k}_{\text{corr-ss}} = P \arg \min_j z_j \quad \text{and} \quad \hat{\epsilon}_{\text{corr-ss}} = P \frac{z_{\hat{k}-1} - z_{\hat{k}+1}}{\frac{N}{M} PK_s}, \quad (4)$$

so that

$$\hat{\tau}_{\text{corr-ss}} = \hat{k}_{\text{corr-ss}} T_{slot} + \hat{\epsilon}_{\text{corr-ss}}, \quad (5)$$

A hybrid scheme may also be considered, which forms the integer estimate from the correlation-superslot method, and the overall estimate using the ML estimate for that particular bin:

$$\hat{k}_{\text{hybrid}} = P \arg \min_j z_j. \quad (6)$$

and

$$\hat{\tau}_{\text{hybrid}} = \hat{\tau}_{\text{ML}, \hat{k}}. \quad (7)$$

The root-mean-squared-error (RMSE) performance of these three schemes as a function of signal flux is shown in Figures 3 for a scenario in which the detected background count rate is 10^5 photoelectrons per second, $M = 16$, $P = 4$, $T_{\text{slot}} = 0.5$ ns, and $N = 10^5$. We see from this plot that the performance of the hybrid scheme approaches that of the ML scheme as the signal flux increases, and that both the hybrid and ML schemes significantly outperform the simple correlation-based method.⁸ We also note that the three estimates exhibit an error floor and do not approach the Cramér-Rao bound. This is because the Cramér-Rao bound is derived for Poisson-distributed observables,⁹ a condition that only applies when the transmitted data sequence is a known deterministic pattern, or if the distribution of each PPM symbol is deterministic over the integration period. When the data is unknown, the observables \mathbf{y} are no longer strictly Poisson, and there is a mismatch with the ML estimator, leading to the error floor. However, the RMSE is still proportional to $1/\sqrt{N}$,⁹ so the error floor may be overcome by longer integration times if necessary.

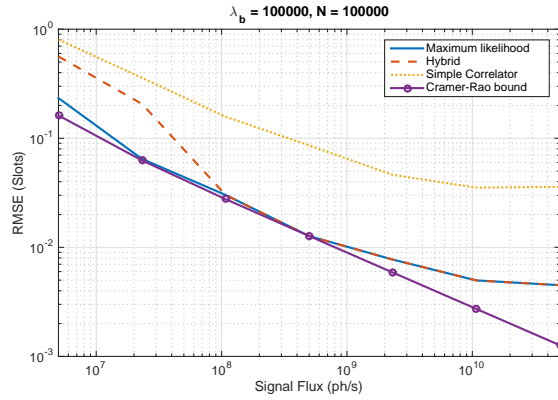


Figure 3: Root mean square error performance of slot timing estimation schemes.

Once a sequence of timing phase estimates are made using one of the methods given here, the frequency offset between the transmitter and receiver clocks may be estimated by estimating the slope of the phase estimate series, using a linear-least-squares fit, for example. A real-time closed-loop implementation of the slot and symbol synchronization algorithm might use the timing offset estimate to drive an error-tracking loop that would make adjustments to the TDC timestamps in order to align them properly to the transmitted slots.

3.3 Log-likelihood Ratio Formation

Once slot and symbol synchronization have taken place, the estimates of slot clock phase and frequency can be used to apportion sparse counts to the correct PPM slot likelihood ratio. The slot likelihood ratio is the ratio of the conditional probabilities that a given slot is or is not a signal slot, and is used in the SCPPM decoding algorithm. For an ideal Poisson counting channel, the likelihood ratio is a function of the slot statistics (detected counts per slot), the mean number of signal counts per symbol K_s , and the mean number of background counts per slot K_b . In addition, knowledge of detector jitter parameters may also be incorporated into the probability model for the log-likelihood ratio in order to further mitigate losses.¹² In order to compensate for this, the log-likelihood ratio (LLR) for slot k of a particular symbol may be modified to interpolate across adjacent slot statistics with weights that incorporate the estimated k -th slot phase offset Δ_k .

$$LLR(k) = \sum_{j=k-D}^{k+D} \mathbf{u}_j \ln \left(1 + f(j, k, \Delta_k, \sigma_j) \frac{\hat{K}_s}{\hat{K}_b} \right) - \hat{K}_s \quad (8)$$

Here, \mathbf{u}_j is the number of timestamps falling within the j th time-of-arrival interval (where the time-of-arrival interval is defined using the current slot clock estimates), and the function $f(j, k, \Delta_k, \sigma_j)$ is a combination of exponentials and Gaussian cumulative distribution functions that depend upon the slot offset estimate Δ_k , the

estimated mean signal and background counts, and the standard deviation of the detector jitter σ_j . D is the number of timestamp intervals that contribute to the LLR, and is a function of the detector jitter. The LLRs only need to be computed for the first M slots of a symbol, and do not need to be calculated for the guard time slots, although photon arrivals in the intersymbol guard time may contribute to the LLRs for the M signaling slots.

The intersymbol guard time may be utilized to estimate the mean background counts per slot, K_b , as

$$\hat{K}_b = \frac{y_{\min}}{N(M+P)(P-1)}. \quad (9)$$

where $y_{\min} = \min\{y_m : 0 \leq m \leq M+P-1\}$. The mean number of signal counts per symbol may then be estimated as

$$\hat{K}_s = \left(\frac{y_{\max}}{(M+P)(M-1)} - N\hat{K}_b \right) \frac{M}{N}. \quad (10)$$

where $y_{\max} = \max\{y_m : 0 \leq m \leq M-1\}$.

The SNSPD array is divided into four quadrants with an equal number of detector pixels, so that a centroid calculation may be performed on the outputs from these four quadrants in order to provide feedback to a line-of-sight stabilization control loop. For forming the LLRs for decoding after spatial acquisition has occurred, estimates of the signal and background counts are made as described above over all of the detector pixels. Prior to spatial tracking, however, estimates of the signal counts are made using Equations (9) and (10) for each detector quadrant.

3.4 Repeat Code Synchronization

The next level of synchronization is that of repeat code synchronization, i.e., estimation of the boundaries of symbol repetitions. Given the set of LLRs formed from the j th slot of the i th repeated symbol $LLR(i, j)$ (where the symbols are repeated Q times), we want to estimate the symbol offset \hat{q} and then sum the repeated symbol LLRs to form the combined LLRs for the j th slot of the k th combined symbol

$$CLLR(k, j, \hat{q}) = \sum_{n=0}^{Q-1} LLR(kQ + n + \hat{q}, j) \quad (11)$$

An intuitive algorithm for estimating the symbol offset that is equivalent to the maximum-likelihood repeat-PPM synchronization method¹³ is to select the offset value that yields the largest average combined LLR corresponding to the hard symbol decisions, i.e.,

$$\hat{q} = \arg \max_q \left(\frac{1}{N} \sum_{n=0}^{N-1} \max_j \{CLLR(n, j, q)\} \right). \quad (12)$$

Here, N is the number of combined symbols used in making the symbol repeat offset estimate.

The performance of this ad-hoc algorithm is shown in Figure 4, which plots the probability of incorrect estimation of the symbol repeat offset value as a function of the mean signal counts per combined symbol for two different operating cases in which repeat factors of four and eight are used to operate links from Venus and Mars, respectively. The value of N used here is 2160, the number of symbols in an SCPPM codeword with $M = 128$. This may be increased in order to improve the probability of repeat sync errors. The plot also shows the codeword error rate under ideal Poisson channel conditions, demonstrating that repeat synchronization may be achieved with high probability at signal levels less than those needed to achieve target codeword error rates.

3.5 Frame Synchronization

Frame alignment sequences (FAS) are inserted between groups of N_c interleaved symbols, where N_c is the number of symbols in a codeword, in order to facilitate deinterleaver and decoder synchronization. The FAS consists of a fixed pattern of N_f PPM symbols that are repeated along with the codeword symbols if symbol repetition is used. In the current implementation, repeat synchronization and symbol combining is performed prior to FAS synchronization and extraction, although they could be performed simultaneously. Three algorithms have been considered for FAS synchronization:

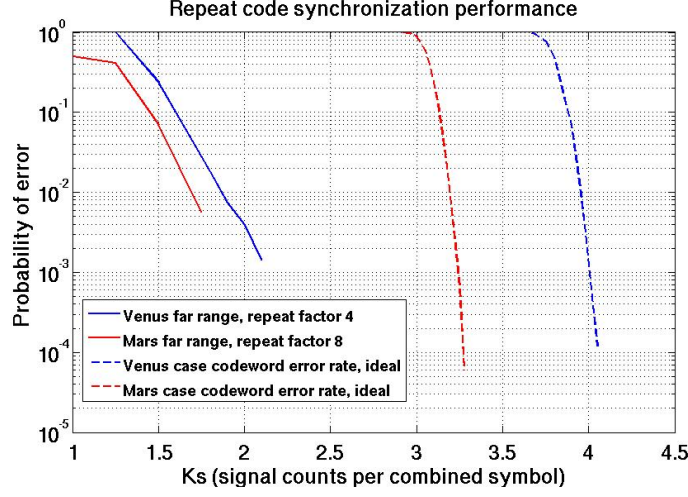


Figure 4: Repeat synchronization error

1. Hard correlation: Hard decisions \hat{s}_k are made for each M -PPM symbol s_k based upon selecting the symbol value corresponding to the maximum slot count. These hard decision values are correlated against the FAS pattern of length N_f , $\{f_0, f_1, \dots, f_{N_f-1}\}$, and the FAS symbol offset estimate is given by

$$C_{hard} = \arg \max_i \sum_{j=0}^{N_f-1} I_{i+j}(f_j), \quad 0 \leq i \leq N_c + N_f. \quad (13)$$

where the indicator function $I_k(f_l)$ is given by

$$I_k(f_l) = \begin{cases} 1, & \text{if } \hat{s}_k = f_l \\ -1, & \text{if } \hat{s}_k \neq f_l \end{cases}.$$

2. Soft correlation: The soft slot count values $\{v(n)\}$ are correlated against a slot representation of the FAS sequence that consists of ones in the pulsed FAS symbol slots and zeros in the nonpulsed slots, and the FAS symbol offset estimate is given by

$$C_{soft} = \arg \max_i \sum_{j=0}^{N_f-1} v(M(i+j) + f_j), \quad 0 \leq i \leq N_c + N_f. \quad (14)$$

3. Maximum likelihood: The ML estimate for the Poisson PPM channel is known,¹⁴ and is simply the soft correlator with a random data adjustment term.

$$C_{ML} = \arg \max_i \sum_{j=0}^{N_f-1} \left[v(M(i+j) + f_j) - \frac{1}{\ln \beta} \ln \sum_{k=0}^{M-1} \beta^{v(M(i+j)+k)} \right], \quad 0 \leq i \leq N_c + N_f. \quad (15)$$

Here, $\beta = 1 + \frac{K_s}{K_b}$.

Note that the correlation sums expressed above are over just one period of FAS insertion. The correlation may be performed over multiple FAS epochs to improve the probability of error. Figure 5 shows performance of the three estimators as a function of mean detected signal counts per symbol for two different scenarios, the first with $M = 16$ and $K_b = 0.0008$, and the second with $M = 128$ and $K_b = 1.24$. For both of these cases, the length of the FAS sequence is $N_f = 16$ PPM symbols. We observe that in the first low background case,

the hard correlator outperforms the soft correlator. In the second higher background case, however, the soft correlator significantly outperforms the hard correlator. The maximum likelihood algorithm outperforms both suboptimal algorithms, and is expected to be used in the DSOC ground receiver. In Figure 5(a) the performance is shown when the number of correlation epochs, L , is either one or two. Increasing the length of the correlation significantly improves performance, at little relative expense in complexity for the ground receiver. We also plot the SCPPM codeword error under ideal Poisson channel conditions and perfect synchronization and parameter estimation in order to demonstrate that the FAS may be acquired in the regime in which decoding is successful, especially if the correlation length is extended to multiple FAS epochs.

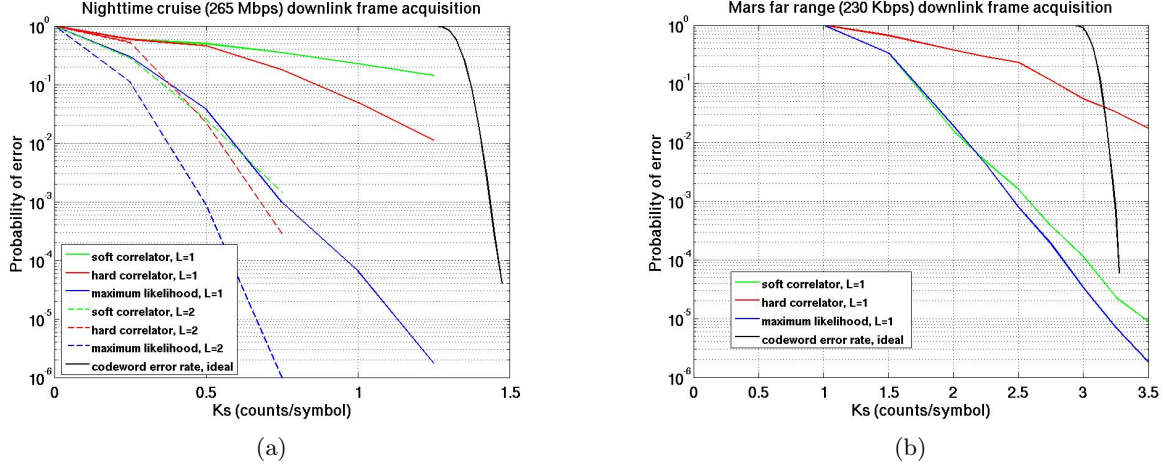


Figure 5: Probability of FAS synchronization error for (a) Nighttime cruise case ($M = 16$, $K_b = 0.0008$), (b) Mars far range case ($M = 128$, $K_b = 1.24$)

Once the codeword frames have been synchronized, the FAS symbols may be removed and the remaining data symbol LLRs may be sent into the convolutional deinterleaver and the SCPPM decoder to extract the transmitted information bits. Convolutional deinterleaving and SCPPM decoding are performed in a straightforward manner.⁷

4. PERFORMANCE RESULTS

The performance of the signal processing algorithms presented here are characterized via Monte-Carlo simulations that include the DSOC modulation and coding format, representative signal and background levels, photodetector modeling including blocking and detector jitter, transmitter clock offset and drift, and signal fading due to transmitter pointing errors. The integrated receiver performance is measured by the decoded codeword error rate, and is compared with the performance of the code in an ideal Poisson channel. The SNSPD array is assumed to have 64 pixels, with each element having RMS detector jitter of $\sigma_j = 0.05$ ns and a blocking time of 40 ns. Detector blocking is modeled as a loss in signal and background flux.¹¹ The time-to-digital converter is assumed to provide a timestamp resolution of 166 ps, and the residual fractional frequency error between the transmit and received clocks is taken to be 0.1 parts per million (we assume that most of the Doppler frequency offset is removed using ephemeris predict data).

Figure 6 shows codeword error rate vs. mean signal counts per symbol for two cases corresponding to nighttime cruise (high rate), and Mars maximum range (low rate) operating points, using SCPPM code rates of 2/3, and 1/3, respectively. Fading is not modeled in these simulations. These plots compare the performance of the receiver with all of the synchronization and parameter estimates described here with the performance of the link in an ideal Poisson channel assuming perfect synchronization and parameter knowledge. In addition, the Shannon capacity threshold is shown along with the expected received downlink signal level assuming a 4 W flight laser transmitter. In Figure 6(a), we observe a 1.2 dB code gap to capacity, 0.75 dB of receiver implementation loss, and a link margin of 5.8 dB, while in Figure 6(b), the code gap to capacity is 0.97 dB, the

receiver implementation loss is 3.4 dB, and the link margin is 4.8 dB. In both cases, more than 3 dB of margin relative to the expected downlink signal power is projected under the simulated conditions.

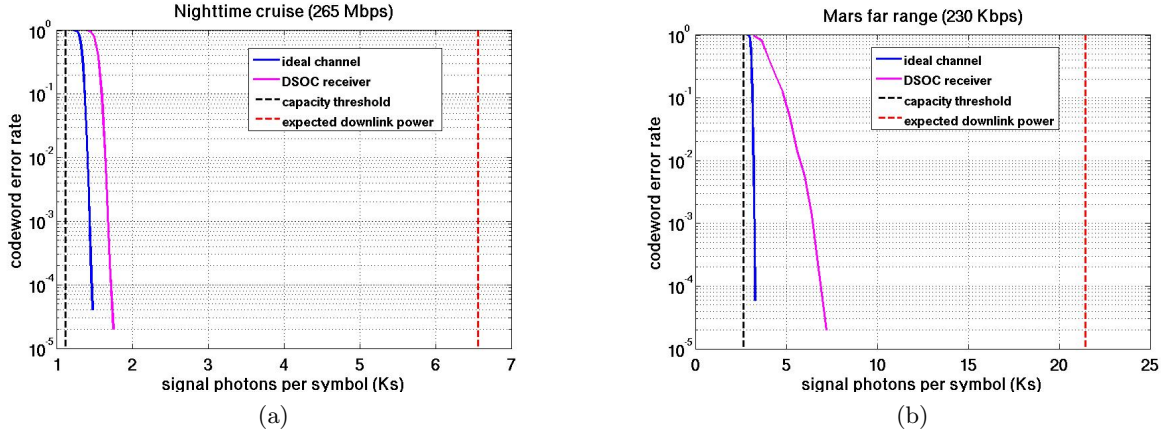


Figure 6: Simulated downlink receiver codeword error rates for (a) Nighttime cruise (b) Mars maximum range

Because the planned DSOC ground receiver aperture diameter is 5 m, the effect of aperture averaging renders the atmospheric-induced fading to be negligible; however, quasi-static downlink pointing errors and time-varying pointing jitter induces a fading process that degrades downlink communications performance.¹⁵ This may be mitigated through the use of channel interleaving. Figure 7 shows the downlink performance for the nighttime cruise case when a pointing-error-induced fading process is included in the channel model. This model assumes a Gaussian pointing error process with static radial pointing bias of $2\mu\text{rad}$ and rms radial pointing jitter of $1.25\mu\text{rad}$, and a coherence time of 100 ms. Note that these pointing error parameters are example values obtained from preliminary simulations of DSOC stressing case pointing errors. Further development and testing will follow to refine these parameters. In the absence of interleaving, this amount of fading is expected to result in a loss of approximately 1.8 dB relative to the unfaded capacity, using previously derived pointing capacity loss formulas.^{15,16} Implementation of channel interleaving and deinterleaving in the receiver is expected to recover about 1.5 dB of this loss based upon the interleaving depth of 2.7 sec that is used here. The simulation results in Figure 7 show a fading loss of approximately 1.6 dB relative to the unfaded receiver performance in the absence of interleaving, and a loss of 0.4 dB when interleaving/deinterleaving is implemented, a recovery of 1.2 dB. Work is in progress to evaluate fading losses and interleaving gain for farther spacecraft ranges.

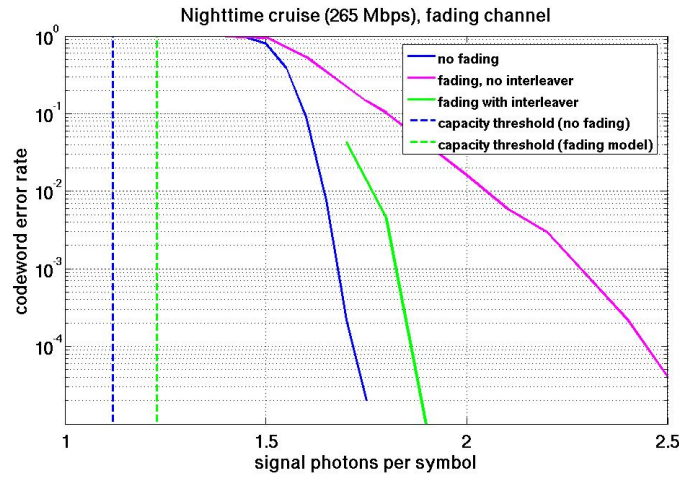


Figure 7: Simulated downlink receiver codeword error rates in the presence of fading and interleaving.

5. CONCLUSIONS

We presented a ground-based receiver concept for demodulating optical PPM waveforms with data rates varying from 50 kbps to 265 Mbps. Algorithms for slot, symbol, and frame synchronization as well as parameter estimation were described, and simulation results for the individual algorithms as well as for the integrated receiver/decoder were presented, showing performance close to downlink budget predictions.⁶ The impact of fading from spacecraft pointing errors on the codeword error rate was evaluated for an example case, both with and without interleaving, demonstrating significant recovery of fading losses as well as reasonably close correspondence with analytical predictions. Next steps in DSOC ground receiver development include laboratory testbed validation of the end-to-end SNSPD detector and timestamp-based receiver performance using software post-processing, to be followed by real-time receiver implementation.

6. ACKNOWLEDGEMENTS

The research described in this publication was carried out at the Jet Propulsion Laboratory, California Institute of Technology, under a contract with the National Aeronautics and Space Administration.

REFERENCES

- [1] Robinson, B. S., Boroson, D. M., Buriyane, D. A., and Murphy, D. V., “The lunar laser communications demonstration,” in *[2011 International Conference on Space Optical Systems and Applications (ICSOS)]*, 54–57 (May 2011).
- [2] Marsili, F., Verma, V. B., Stern, J., Harrington, S., Lita, A. E., Gerrits, T., Vayshenker, I., Baek, B., Shaw, M. D., Mirin, R. P., and Nam, S. W., “Detecting single infrared photons with 93% system efficiency,” *Nature Photonics* **7**, 210–214 (February 2013).
- [3] Shaw, M., Marsili, F., Beyer, A., Stern, J., Resta, G., Ravindran, P., Chang, S. W., Bardin, J., Patawaran, F., Verma, V., Mirin, R. P., Nam, S. W., and Farr, W., “Arrays of WSi superconducting nanowire single photon detectors for deep space optical communications,” in *[CLEO: 2015]*, *CLEO: 2015*, JTh2A.68, Optical Society of America (2015).
- [4] Willis, M. M., Robinson, B. S., Stevens, M. L., Romkey, B. R., Matthews, J. A., Greco, J. A., E. Grein, M., Dauler, E. A., Kerman, A. J., Rosenberg, D., Murphy, D. V., and Boroson, D. M., “Downlink synchronization for the lunar laser communications demonstration,” in *[2011 International Conference on Space Optical Systems and Applications]*, 83–87 (May 2011).
- [5] Baumann, T., Bchele, M., Fischer, H., Gorzellik, M., Grussenmeyer, T., Herrmann, F., Jrg, P., Knigsmann, K., Kremser, P., Kunz, T., Michalski, C., Schill, C., Schopferer, S., and Szameitat, T., “The GANDALF 128-channel time-to-digital converter,” *Journal of Instrumentation* **8**(1), C01016 (2013).
- [6] Biswas, A., Hemmati, H., Piazzolla, S., Moision, B., Birnbaum, K., and Quirk, K., “Deep-space optical terminals systems engineering,” *IPN Progress Report* **42** (November 2010).
- [7] Moision, B. and Hamkins, J., “Low-complexity serially-concatenated coding for the deep space optical channel,” in *[Proceedings of the 2003 IEEE International Symposium on Information Theory (ISIT)]*, (June 2003).
- [8] Quirk, K. J., Gin, J., and Srinivasan, M., “Optical PPM synchronization for photon counting receivers,” in *[IEEE Military Communications Conference, MILCOM]*, 1–7 (Nov. 2008).
- [9] Rogalin, R. and Srinivasan, M., “Maximum likelihood synchronization for pulse position modulation with inter-symbol guard times,” *Proceedings of IEEE Globecom 2016* (December 2016).
- [10] Gagliardi, R. M. and Karp, S., *[Optical Communications]*, John Wiley & Sons, New York, New York, 1st ed. (1976).
- [11] Moision, B. and Piazzolla, S., “Blocking losses on an optical communications link,” *2011 International Conference on Space Optical Systems and Applications (ICSOS)*, 368–377 (May 2011).
- [12] Quirk, K. J. and Srinivasan, M., “Optical PPM demodulation from slot-sampled photon counting detectors,” in *[MILCOM 2013 - 2013 IEEE Military Communications Conference]*, 1634–1638 (Nov 2013).
- [13] Connelly, J., “Repeat-PPM super-symbol synchronization,” *IPN Progress Report* **42** (November 2016).

- [14] Georgiades, C. N. and Snyder, D. L., “Locating data frames in direct-detection optical communication systems,” in [*IEEE Transactions on Communications*], **COM-32**, 118–123 (February 1984).
- [15] Barron, R. J. and Boroson, D. M., “Analysis of capacity and probability of outage for free-space optical channels with fading due to pointing and tracking error,” *Proc. SPIE* **6105**, 61050B–61050B–12 (2006).
- [16] Moision, B., Wu, J., and Shambayati, S., “An optical communications link design tool for long-term mission planning for deep-space missions,” in [*2012 IEEE Aerospace Conference*], 1–12 (March 2012).